Journal of Power Sources 626 (2025) 235784

Contents lists available at ScienceDirect

Journal of Power Sources

journal homepage: www.elsevier.com/locate/jpowsour

Aluminum-air batteries with acidic bio-polymer gel electrolytes and wood-derived metal-free cathodes

M.F. Gaele, P. Gargiulo, T.M. Di Palma *

CNR-Istituto di Scienze e Tecnologie per La Mobilità Sostenibile, Viale G. Marconi 4, 80125, Naples, Italy

HIGHLIGHTS

- Al-air cells have been made with acidic GPEs and different cathodes.
- The wood-derived cathodes exhibit lower R_{ct} and mass transport impedances.
- The gravimetric capacity is 2682 mAh g^{-1} at 1 mA cm^{-2} discharge current.

GRAPHICAL ABSTRACT

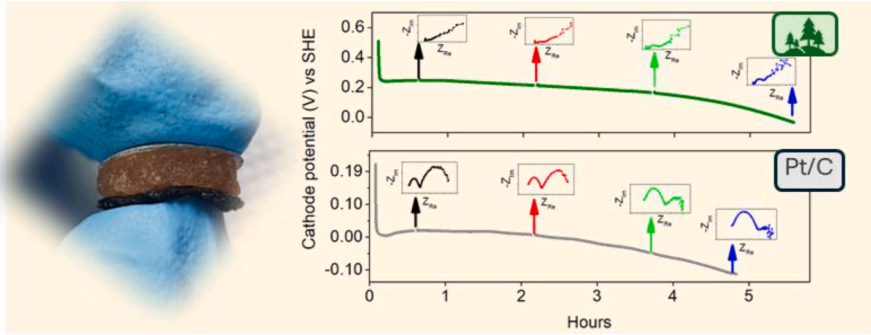

ARTICLE INFO

Keywords:
Al-air batteries
GPE
Acidic electrolytes
Cathodes

ABSTRACT

Aluminum-air batteries with acidic xanthan-based gel polymer electrolytes and metal-free cathodes made of wood-derived activated carbons have been prepared and their electrochemical performances have been compared with those of the same cells assembled with benchmark platinum/carbon cathodes. Three-electrode electrochemical tests made possible to decouple the anodic and cathodic contributions during the functioning of the cells, allowing unambiguous interpretations of the electrode processes. Compared to the platinum/carbon cathodes, the cathodic potentials of the cheaper wood-derived cathodes show higher values, responsible for the enhanced cell potentials. The galvanostatic impedance spectroscopy carried out at different discharge currents and during discharge tests highlighted a lower impedance for both the charge transfer reaction and the mass transport phenomena of the activated carbon compared to the platinum/carbon one. We found that cells made with xanthan-based polymer gel electrolyte and wood-derived activated carbon have stable potentials at around 1 V @ 1 mA cm^{-2}, moderate capacity of about 25 mAh cm^{-2} and gravimetric capacities that can reach the outstanding value of 2682 mAh g^{-1} even at low discharge currents.

* Corresponding author.
E-mail address: tonia.dipalma@stems.cnr.it (T.M. Di Palma).

https://doi.org/10.1016/j.jpowsour.2024.235784
Received 27 August 2024; Received in revised form 14 October 2024; Accepted 4 November 2024
Available online 11 November 2024
0378-7753/© 2024 The Authors. Published by Elsevier B.V. This is an open access article under the CC BY license (http://creativecommons.org/licenses/by/4.0/).

1. Introduction

Metal-air batteries are electrochemical energy conversion devices that are considered promising alternative to the current lithium-ion batteries [1,2]. They are based on redox reactions between metals and atmospheric oxygen that reversibly form solid metal oxides. These devices are less expensive and may present high theoretical capacities. In this context, it is of particular interest the development of "multivalent" batteries where the anode is made of metals such as Al, Zn, Fe, Sn which release more than one electron in the oxidation, thus producing huge advances in energy density with the additional benefit of using cheaper and more abundant components than lithium [3,4]. To work, these batteries require a metal anode, an electrolyte (aqueous or non-aqueous) and a porous conductive cathode on which a catalyst, which allows the reactions of atmospheric oxygen, is dispersed [5,6]. During the discharge the metal oxidizes and the oxygen is consumed on the cathode forming an oxide or hydroxide as a product of the final reaction. Reversibly, during the charge, the reaction products decompose and the oxygen is released from the same electrode [7].

Among the various metals used as anodes in metal-air batteries, aluminum is the material with the most promising parameters in terms of economy, eco-sustainability and electrochemistry at the same time. Indeed, aluminum is the most abundant metal in the Earth's crust, it is produced with consolidated technologies and has a well-tested recycling chain. At the same time, an aluminum anode has a specific theoretical capacity of 2.98 Ah g^{-1}, which corresponds to 77 % of that one of lithium.

Aluminum-air (Al-air) batteries can operate with different electrolytes, aqueous or non-aqueous, and at different pH [8]. The Al-air cells of higher power are made with aqueous alkaline electrolytes [9]. However, in alkaline media aluminum corrodes severely and forms hydroxides. On the other hand, in these electrolytes, aluminum hydroxide is also the product of the electrochemical reaction. When the electrolyte solution is saturated, the hydroxide precipitates, forming a solid oxide layer on the anode and preventing the cell from supplying further electricity. This issue is particularly critical when solid or quasi-solid gel polymer electrolytes (GPEs) are used. In this case, solid reaction products may clog the electrolyte causing a rapid cell failure. The strategies used to enhance the performances of Al-air alkaline cells are mainly based on the mitigation of self-corrosion, using suitable additives in the electrolytes [10] or aluminum alloys [11].

GPEs are preferred to liquid electrolytes due to their higher stability and capability to reduce corrosion [12,13]. In some previous works, we demonstrated the functioning of Al-air cells using gel polymer electrolytes based on natural polysaccharides, namely xanthan gum, and aqueous acidic solutions [14,15]. Xanthan gum is a branched bacterial polysaccharide produced by secretion from the bacterium *Xanthomonas campestris* in aerobic fermentation conditions. It is widely used as a food additive [16] and gelling agent in the cosmetic and pharmaceutical industry [17,18]. We found that xanthan gum is a valuable polymer for the production of aqueous gel electrolytes as, depending on the solution pH, it may form sticky, gummy or really sturdy hydrogels [8,14,15,19,20].

In concentrated acidic solutions, xanthan can generate solid rubbery hydrogels that are rigid enough to be sliced. This stiffness is due to the cross-linking of polymer chains, which results in a three-dimensional structure capable of capturing water molecules [15]. In acidic solutions, cross-linking can occur through hydrogen bonds directly between different chains or through water molecules as bridges. In fact, in a strongly acidic medium, all carboxylate groups of xanthan are in protonated form, then they can form direct hydrogen bonds between C=O and OH of different chains, creating a strong physically cross-linked hydrogel [15].

The acidic Xanthan-based hydrogels have a high ionic conductivity, which makes the relative Al-air batteries particularly interesting, since they are characterized by confrontable or even higher capacities than those made with the Xanthan-based alkaline gel polymer electrolytes. This is due to two main remarkable properties of aluminum anode contacted with these GPEs, namely the higher solubility of the reaction product Al^{3+} that reduces electrolyte clogging and the inhibition of aluminum self-corrosion by the xanthan protective layer on the metal surface [14]. This latter aspect was studied by the authors in a previous work, by performing potentiodynamic polarization curves on aluminum anodes contacted with acidic xanthan-based GPEs at different xanthan and hydrochloric acid concentrations. The corrosion inhibiting effect was clearly observed by the progressive shift of the corrosion potential towards more negative values and by the lowering of corrosion currents when gels were used as electrolytes instead of liquid acid solutions [14].

The half-reactions of the Al-air battery using aqueous acidic electrolytes are described by the following equations:

$$\text{Anode } Al^{3+} + 3e^- \rightarrow Al \quad E^0 = -1.66\ V \tag{1}$$

$$\text{Cathode } O_2 + 4H^+ + 4e^- \rightarrow 2H_2O \quad E^0 = 1.23\ V \tag{2}$$

The overall reaction is given by:

$$Al + \frac{3}{4}O_2 + 3H^+ \rightarrow Al^{3+} + \frac{3}{2}H_2O \qquad E^0 = 2.89\ V \tag{3}$$

while the self-corrosion reaction is

$$Al + 3H^+ \rightarrow Al^{3+} + \frac{3}{2}H_2 \tag{4}$$

In addition, as the standard potential of the cathodic reaction in acidic solutions (Eq. (2)) is higher than that one in alkaline solutions ($E^0 = 0.8\ V$), acidic electrolytes may also find application in Al-air batteries as catholytes in dual or three-electrolyte cell configurations in order to increase the cell voltage [21–25].

Previously, we used commercial materials made of platinum dispersed on carbon (hereafter Pt/C) to fabricate cathodes for Al-air batteries [26]. In view of preparing cheaper Al-air cells, we recently moved to the production of cathodes made of activated carbons of natural origin, and we demonstrated that they are more efficient than Pt/C cathodes in alkaline Al-air batteries [26]. Furthermore, we demonstrated that these cathodic materials were also effective in Al-air cells assembled with Xanthan-based saline aqueous electrolytes [19]. The operation of the neutral cells, with capacities between 12 and 20 mAh cm^{-2} and energy density of about 12 mWh cm^{-2}, was optimized for a range of 1–2 mA cm^{-2}. Due to their intrinsic feature of safety and sustainability, these cells are particularly suitable for powering disposable biomedical devices [19].

The benefit of using agricultural waste instead of precious metals to produce materials to enhance the ORR reaction is undoubted and it goes far beyond the economic one. It is sufficient to mention that platinum is designed as a "critical raw material" by the European Commission [27]. Similarly, the "critical raw materials" list includes rare earths or cobalt, namely the elements which are currently used for ORR catalysis. These materials are classified as "critical" mainly because they are predominantly found in limited areas of the planet that, in some cases, are characterized by high geopolitical instability. In addition, their extraction and processing involve a high environmental, social, and economic impact that needs to be carefully evaluated across various scenarios [28]. Instead, agricultural wastes are widespread and are sustainable precursor to materials used in the energy sector [29].

Here we analyze the electrochemical performances of Al-air cells produced with Xanthan-based acidic electrolytes using wood-derived carbon-based cathodes. We tested the electrochemical features of the cathodes contacted with acidic electrolytes through linear sweep voltammetry (LSV) and three-electrode galvanostatic electrochemical impedance spectroscopy (EIS), while cell electrochemical performances were evaluated through polarization measurements and discharge tests. The results demonstrate that these carbonaceous materials show lower impedances toward the charge transfer reactions and the mass transport.

Their combined use with xanthan-based electrolytes may enable low-cost Al-air batteries with gravimetric capacity values up to the outstanding 2682 mAh g^{-1} and maximum energy density value of 2700 Wh Kg^{-1}.

2. Materials and methods

The acidic gel polymer electrolytes were prepared by fast mixing followed by a 5-min vigorous kneading of xanthan gum powders (powders from Xanthomonas campestris, Merck) in 5M hydrochloric acid (HCl) solution at four different ratios, namely 500, 700, 900 and 1400 mg mL^{-1}. The percentage of the liquid content (weight) in the electrolytes was 68 %, 61 %, 54.5 % and 43.5 %, respectively.

The obtained materials were homogeneous, brownish and gummy gels, sturdy enough to be sliced with a knife or shaped with hallow cutter punches, and with good elastic behavior (Fig. S1). The gels were named 50Xa, 70Xa, 90Xa and 140Xa, respectively (Fig. 1, top-left). Immediately after preparation, the gels were closed in plastic containers and used after resting at room temperature for at least 24 h. All gels were stored at room temperature (20–25 °C) and remained stable up to 3 months (50Xa) and over 8 months (70Xa and 90Xa). In Table 1 the weight percentages of water, HCl and xanthan in the different gels are reported.

Air cathodes were prepared by using 13 mm diameter discs in carbon cloth (H2-Planet, 0.35 mm thick, 116 g m^{-2}) as supports on which the carbon suspensions were spread. The suspensions were prepared by mixing polyvinylidene fluoride (Merck, powder form) with carbon powders in a weight ratio of 1:10, and by adding 1 cm^3 of solvent (1-methyl-2- pyrrolidinone, Merck) per 220 mg of solid mixture. The carbon powders used for the suspensions were activated charcoal produced from wood (product number 05105, Merck, hereafter named AC1) and platinum-dispersed activated carbon (Pt/C, 10 wt % Pt, provided by Merck in powder form). After drying at 80 °C for 4 h, the final Pt concentration in the Pt/C cathodes was 2.5 % wt. of the cathode's total weight. The amount of carbon pasted on each cathode was about 12 mg, while the total weight of the cathodes was about 45 mg. The final cost of the wood-derived carbon is less than the 2 % of the platinum-dispersed carbon (Table S1).

Table 1
Weight percentages of water, hydrochloric acid and xanthan in the tested gels.

Gel components	Weight (%)			
	50Xa	70Xa	90Xa	140Xa
Water	57	51	45.5	36.5
HCl	11	10	9	7
Xanthan	32	39	45.5	56.5

Ultrapure aluminum (Puratronic, 0.5 mm thick, 99.998 %, Alfa Aesar) was used as the anode in the form of a 13-mm diameter disc. The weight of the anodes varied between 150 and 170 mg.

The Al-air cells were assembled by contacting the gel electrolytes between anode and cathode by using 3 mm rigid spacers. It is worth noting that, although the use of rigid spacers ensures greater reproducibility in the measurements, it tends to reduce the cell capacity due to the loss of contact when the electrolytes start to dry out and shrink during the discharge. The weight of the gel polymer electrolytes used in the cells was about 600 mg. The liquid amount in 600 mg of GPE was about 0.38 mL, 0.34 mL, 0.3 mL and 0.24 mL for 50Xa, 70Xa, 90Xa and 140Xa, respectively.

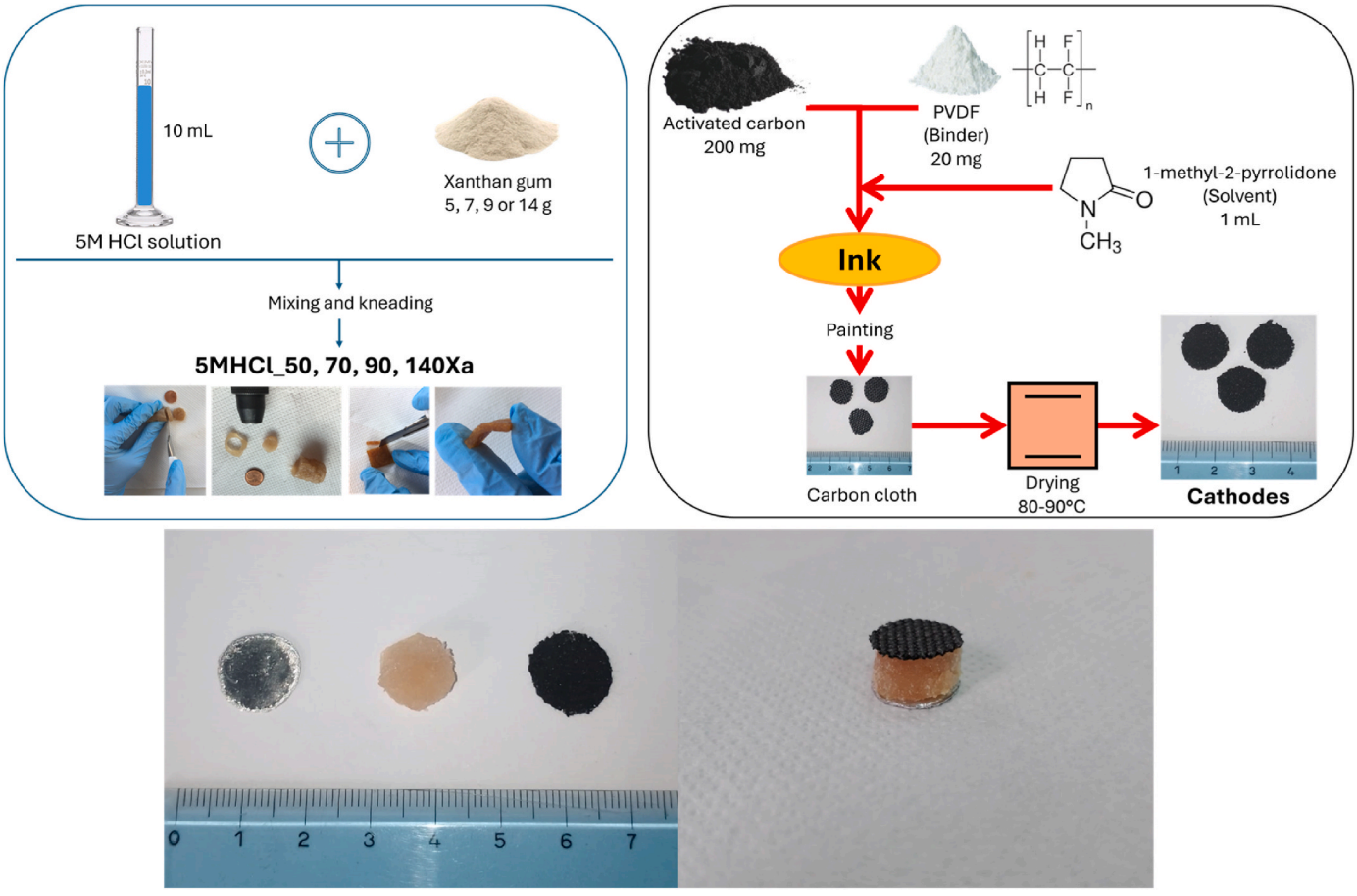

Fig. 1. Material preparation and cell assembly. Top-left: Preparation procedure of the hydrogels; Top-right: Preparation procedure of the cathodes; Bottom-left: Components of a 13 mm-diameter acidic Al-air cell; Bottom-right: Assembled acidic Al-air cell.

The Al-air cells assembled with the different gel polymer electrolytes were named nnXa-cell, were nn = 50, 70, 90 or 140.

Fig. 1 shows the scheme of the material preparation and cell assembly procedures.

An evaluation of costs of acidic Al-air cells made with the different cathodes is reported in Table S1. The electrochemical characterizations were performed by using a Zahner Zennium and an Autolab PGSTAT302N electrochemical workstations. The oxygen reduction reaction (ORR) performances of AC1 and Pt/C cathodes contacted with solid acidic electrolytes and the gel electrochemical stability were evaluated through I-V curve analysis and cyclic voltammetry measurements, respectively. The I-V measurements were carried out by using a three-electrode cell setup where the cathode was the working electrode, a 1 cm^2 platinum plate was the counter electrode and Ag/AgCl (saturated KCl) was the reference electrode. The I-V curves were acquired by starting from the open circuit voltage (OCV) and by varying the potential towards more negative values at scan rate of 1 mV s^{-1}. The cyclic voltammetry curves were performed by using a three-electrode setup with glassy carbon as working electrode, a platinum plate as counter electrode and Ag/AgCl (saturated KCl) as reference electrode. The curves were recorded in the range from −1.5 V to +1.5 V with a scan rate of 10 mV s^{-1}. The discharge measurements were conducted both in two- and in three-electrode configuration by using Ag/AgCl electrode. The electrochemical impedance spectroscopy (EIS) measurements were performed in two-electrode configuration, potentiostatic mode and in a three-electrode cell configuration by setting the workstations in galvanostatic mode (1 MHz–10 mHz, 100 μA amplitude perturbation). The conductivity values of the electrolytes were obtained from the formula

$$\sigma = {}^{L}/_{R_{el}A} \tag{5}$$

where L and A are the thickness and the contact area of the samples, respectively, and R_{el} is the electrolyte resistance, which was retrieved from the intercept of the Nyquist plot with the real axis.

The morphological and elementary analysis of the samples were performed with a scanning electron microscope (SEM, Phenom ProX) equipped with an energy-dispersive X-ray spectrometer (EDX) detector. An Alpha 3–4 LSC basic – Christ Freeze Dryer was used for samples drying. A Mettler Toledo TGA/DSC 3+ thermogravimetric analyzer was used for the gel thermal analysis in 80 mL min^{-1} nitrogen flow (25–800 °C temperature range, 10 °C min^{-1} heating rate). IR spectra were recorded by using an Agilent Cary 630 FTIR spectrometer equipped with an Attenuated Total Reflection (ATR) accessory in a scanning range of 4000–650 cm^{-1} (resolution 2 cm^{-1}, 64 scan).

Weight loss measurements of GPEs were performed in order to evaluate the evaporation of liquid solution. Approximately 1.2 g of hydrogel, for each sample, were exposed to air at ambient conditions of temperature and humidity and the weights were recorded for about 3 days.

After discharge tests, anodes were not covered by visible oxide layers, as also confirmed by SEM-EDX analysis (Figs. S2–S4). This allowed reliable anodic efficiency measurement, at different discharge current, through weight loss methods. Hence, before and after the discharge test, the anodes were gently cleaned with bi-distilled water and dried with soft paper and the anodic efficiencies η were retrieved by using the equation

$$\eta = 100 \times \frac{M_{Al} \times I \times t}{3 \times F \times \Delta W} \tag{6}$$

where I is the discharge current density (A), t is the discharge time (h), M_{Al} is the molar mass of aluminum, F is the Faraday constant and ΔW (g) is the mass difference of the metal anode before and after the discharge.

3. Results and discussion

3.1. Materials characterization

In Fig. 2a the FTIR spectrum of 70Xa fresh acidic gel is reported and compared with the spectra of Xanthan powders, 70Xa two-month aged gel, 70Xa dried gel and a water-based xanthan gel, named 80Xa_H_2O, whose water amount is comparable with that one of the 70Xa hydrogel. The analysis of this water-based hydrogel was carried out to evaluate the separate contributions of water and hydrochloric acid to the physicochemical characteristics of the hydrogels. A broad absorption peak at 3300 cm^{-1} is due to the O−H stretching vibration of hydroxyl groups. The peaks at 1718, 1602, 1400, and 1020 cm^{-1} for xanthan gum can be attributed to carbonyl group stretching of -COOH, asymmetrical and symmetrical C=O stretching of carboxylate anion (-COO^-) and C−O stretching of alcoholic group, respectively [30]. In Table 2 the main peaks of the FTIR spectra are reported.

The major differences between the samples are mainly observed in the range 800–2000 cm^{-1}. More specifically, with respect to the xanthan spectrum, an additional peak can be observed at 1054 cm^{-1} in the spectra of gels containing water. This new band may be due to solvation effects on C-O stretching of alcoholic groups, i.e. hydrogen bonds between water and -OH of the alcoholic groups. Moreover, the band at 1602 cm^{-1} is shifted of about 30 cm^{-1} in all the gels spectra. Also, in this case, an effect of solvation can be invoked, i.e. the formation of hydrogen bonds between carboxylate anions (-COO^-) and water. Finally, in the dried gel sample, the intensity of the peak at 1718 cm^{-1} becomes higher with respect to the signal at 1634 cm^{-1}, indicating that in absence of water, the presence of carboxylic groups is prevalent with respect to carboxylate ones.

Fig. 2b and c shows the TGA and DSC thermograms of a 70Xa gel, compared with the aged gel, the bare polymer, and the 80Xa_H_2O gel. The xanthan curve shows two weight losses, at 70 and 280 °C, endothermic and exothermic, respectively. The first loss is associated with residual moisture in the polymer powder, while the second one corresponds to xanthan exothermic decomposition (red curve in Fig. 2b). The sample prepared with xanthan and neutral water (80Xa_H2O) presents a more evident loss at 70 °C, but a less intense signal of xanthan decomposition, due to the incipient gel formation. The gel used as electrolyte (70Xa) shows a different thermal behavior. In particular, two strong weight losses are observed, at 90 and 115 °C. The first one can be attributed to the loss of acidic water, weakly and externally surrounded to the crosslinked gel structure, while the rapid weight loss at 115 °C is associated with the acidic water enclosed inside the gel structure. Finally, the aged sample shows the same thermograms of the fresh electrolyte [15], indicating that an aging at room temperature for two months does not affect the thermal stability of the electrolyte.

In Fig. 2d the weight loss curves due to the solution evaporation are reported. From the comparison of the curves, for the first 10 h, no significant differences are observed as a function of xanthan concentration. Then, a small difference can be observed for the 90Xa gel with respect to the other hydrogels, which is justified by the lower liquid amount contained in this hydrogel, as shown in Table 1. Whereas, 50Xa and 70Xa curves are overlapped during the entire measurement. In addition, considering that the gels initially contain an amount comprised between 0.6 and 0.8 g of liquid solution, the figure shows that after 72 h the gel still retains half of the solution.

In Fig. 2e, the CV figures are reported. The inflection toward negative current starting at −0.8 V and towards positive current at +1.3 V are due to hydrogen and oxygen evolution, respectively. Despite the high molarity of the acidic solution in the gels, inflections toward negative current at 0 V, corresponding to the H^+ reduction are not detected.

EIS measurements, which were performed to evaluate the ionic conductivity of the electrolytes at different solid/liquid ratios, are reported in Fig. 2f and Table S2. Although the electrolytes prepared with xanthan are quasi-solid materials, the conductivity values are quite high,

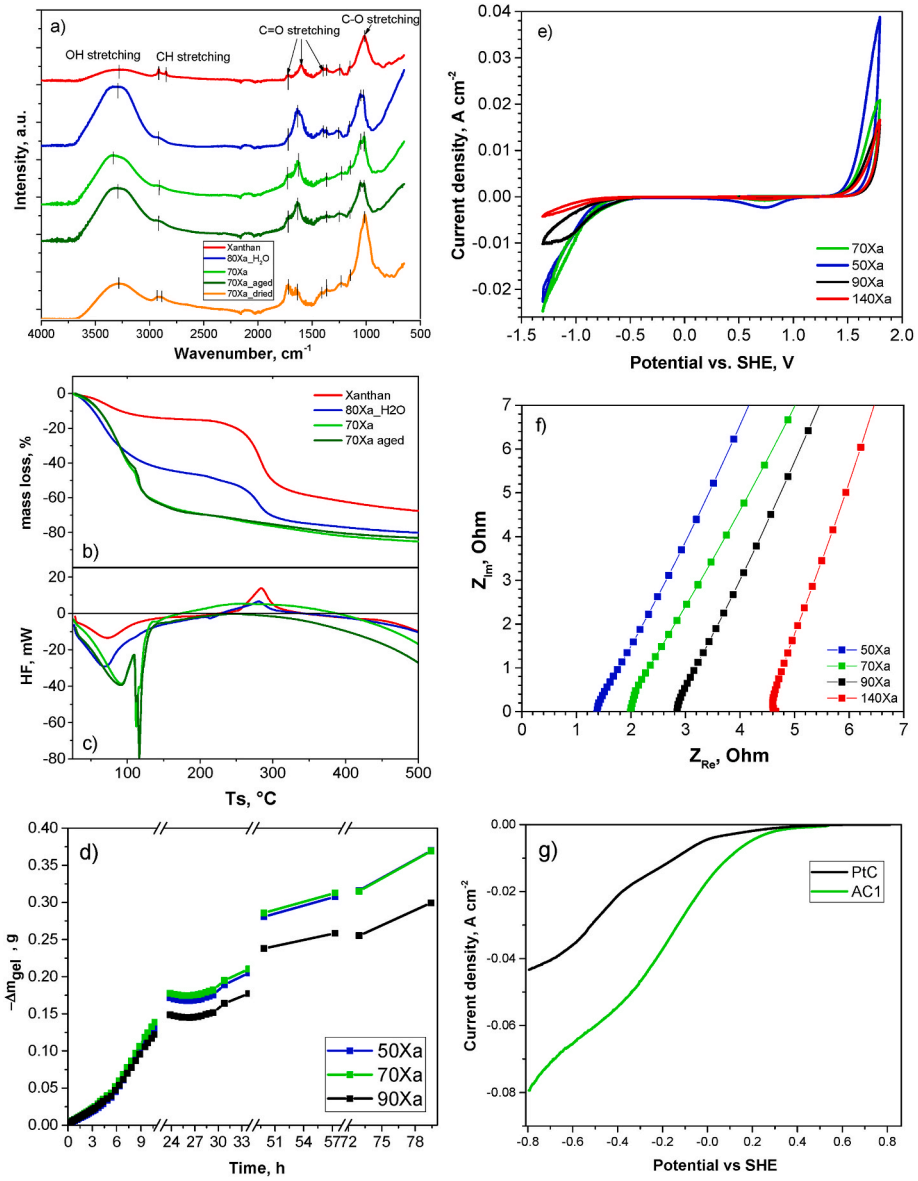

Fig. 2. a) FTIR-ATR spectra; b) TGA curves; c) DSC curves; d) Weight loss curves due to evaporation; e) CV curves performed on the tested gels; f) EIS curves (Nyquist plot) comparison between the hydrogels with AC1 cathodes; g) LSV curves performed on 70Xa gel electrolyte and AC1 or Pt/C cathodes.

Table 2
FTIR absorptions of different materials by frequency regions.

Materials	cm^{-1}			
	OH stretching	CH stretching	C=O stretching	CO stretching
Xanthan	3265	2916–2847	1718-1602-1399	1017
80Xa_H_2O	3338	2919	1718-1636-1400	1054–1030
70Xa	3336	2935	1717–1635	1053–1018
70Xa_aged	3302	2931	1717–1635	1054–1022
70Xa_dried	3277	2930–2891	1718–1653	1013

ranging from 0.04 to 0.13 S cm^{-1} (Table S2). The 50Xa electrolyte containing the highest liquid concentration shows the highest conductivity value, that is less than one order of magnitude of the 5M HCl solution [31]. The ionic conductivity value of the xanthan most concentrated sample, 140Xa, is reduced by more than two thirds, but it can be still sufficient for low-power electrochemical applications.

After the discharge the ionic conductivity of the electrolyte is reduced of an order of magnitude, becoming unusable for the reuse of the cell (Fig. S13).

The catalytic activity of cathodic materials can be evaluated through linear sweep voltammetry (LSV) studies. Through an LSV the rate of an electrochemical reaction on an electrode is monitored by performing a potential scan which, in the case of ORRs, is from the OCP towards more negative potentials. However, the rate of the ORRs on porous, carbonaceous electrodes, depends not only on the intrinsic activity of the material towards oxygen reaction but also on the mass transport through the electrode. Rigorously, to decouple the processes, it would be necessary to use a spinning disk electrode setup apparatus and kinetic models based on the Koutecky-Levich (K-L) equation [32,33]. However, LSV measurements effected directly on cathodes in contact with solid electrolytes allows to evaluate the ORR performances of the cathodes used in GPE metal-air batteries in more practical conditions. In addition, as the electrolyte is a quasi-solid material, the polarization effects are different from those generated under more controlled conditions such as in measurements made with the rotating disk. Thus, the polarization could alter the typical S-shape of LSV. Anyway, it is acknowledged that

some features of the LSV curves are qualitative indicators of the activity of the cathodic materials towards the reactions with oxygen. In fact, at cathodic potentials very close to the OCV, the overpotential may be insufficient to overcome the reaction barrier and to achieve a substantial rate of the electrochemical reaction. Therefore, the reaction rate is very slow and a plateau in the LSV is recorded. When the potential is increased towards more negative values, the reaction rate increases, and this determines an increase in the recorded current. A marked variation of the slope in the LSV curve occurs at specific potential E_{onset} values. The E_{onset} can be used as a qualitative indicator of the activity of the cathodic material towards the ORR and of the efficiency of the cathode in the cell: the closer the E_{onset} is to the OCV, namely the more reduced the overpotential is, the more the cathodic material is active and the more the cathode is efficient in the electrochemical cells.

In Fig. 2g the LSV curves of the Pt/C and AC1 cathodes contacted with 70Xa are reported. The curves were acquired from the OCP to −0.8 V vs SHE. The further negative increasing of the potential was not considered because the LSV curves could show the effect of other reduction reactions than the ORR such as direct water reduction. It results that the onset of the LSV curves recorded for the AC1 cathode is shifted to more positive potentials, indicating its better ORR performance.

3.2. Cell electrochemical characterization

In order to compare the cells assembled with different cathodes and electrolytes, polarization/power curves were recorded, and V/I rate performance discharge measurements were conducted by using a three-electrode configuration. The results of the tests are reported in Fig. 3.

From Fig. 3 left, it is shown that a lower polymer concentration reduces the polarization at higher current densities, likely due to the better wettability of the electrodes, as well as the increased electrolyte conductivities. In all cases, the cells assembled with AC1 cathodes show increased potentials and powers with respect to those made with Pt/C cathodes. Notably, the 50Xa-cell assembled with the AC1 cathode shows twice the power of the respective cell made with the Pt/C cathode.

The results of the three-electrode discharge tests at different currents, performed using Ag/AgCl as the reference electrode, are shown in Fig. 3 right. This test allows to measure the cathodic and anodic potentials and to evaluate the effect of the polarization on each electrode. The polarization is due to the depletion or accumulation of charge carriers on the electrodes and lowers the cell voltage. The extent of polarization is described by the overpotential which, in a galvanic cell, determines a less negative potential on the anode and a less positive one on the cathode [34]. The evaluation of the overpotential on each electrode allows a better understanding of the phenomena at the electrode interface which can influence the overall electrochemical cell performance, thus guiding the construction of more efficient cells. The test was carried out by comparing 70Xa-cells made with the two different cathodes, and the 50Xa, 90Xa and 140Xa-cells assembled with the AC1 cathode. All the cells assembled with AC1 cathodes show higher cell potentials, from 0.2 to 0.4 V depending on the discharge current, with respect to that assembled with the Pt/C cathode. As results from the figure, this effect is mainly due to the different cathodic potentials of the cell assembled with Pt/C that results more negative. This indicates that, in the cells assembled with AC1 cathodes, the electrons produced by the oxidation of the metal are more effectively neutralized in the oxygen reduction reaction. This is due to the combined effect of the key features of materials constituting the positive electrode in a metal-air cell, as porosity, electrical conductivity, and catalytic properties for oxygen reactions [35]. In a previous paper we studied the properties of the carbonaceous materials of which the two cathodes, AC1 and Pt/C, are made [26]. In Ref. [26], we reported that, while the Brunauer–Emmett–Teller (BET) analysis showed hierarchical porosity and almost comparable surface areas for both materials, the Raman spectroscopy analysis, instead, highlighted a higher structural order and graphitization degree of AC1. Therefore, the carbonaceous powders of which AC1 is made could be electrically more conductive than the other samples [35]. Furthermore, in the Raman spectrum of AC1, the band shift at 1550 cm^{-1} may be related to specific defects or doping [36] which are associated with catalytic properties in these materials. LSV measurements on AC1 contacted with alkaline [26], saline [19], as well as acidic electrolytes (Fig. 2g) showed more positive onsets with respect to Pt/C cathodes contacted with the same electrolytes.

By considering the potentials as a function of the Xanthan concentration, the electrolyte giving the best cell performances is the 50Xa

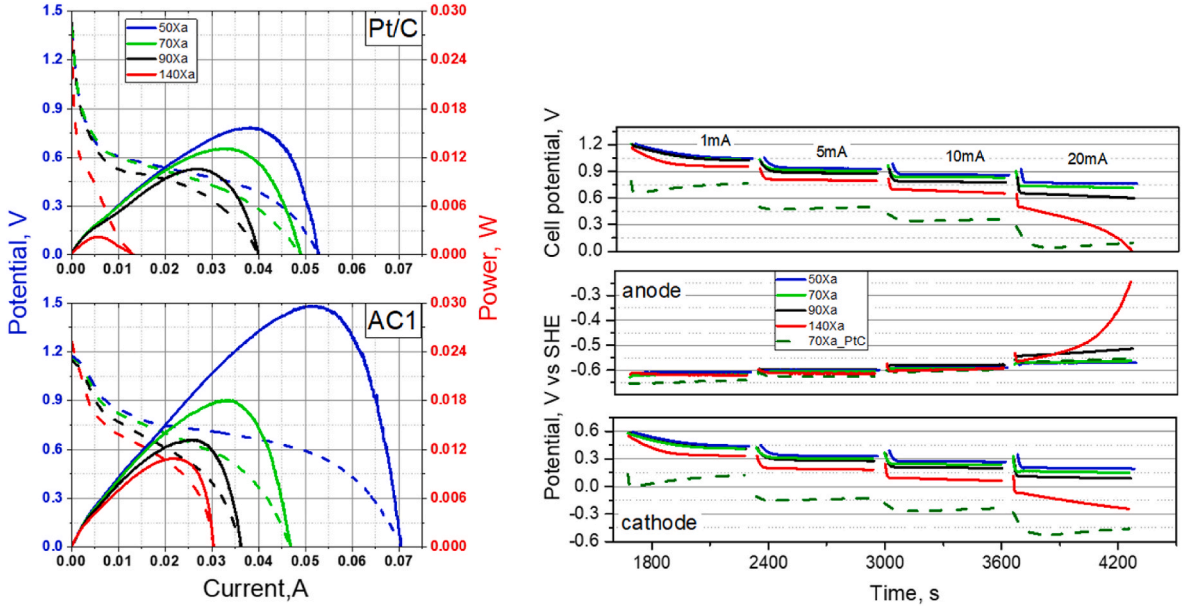

Fig. 3. Polarization-power curves and V-I rate performance discharge tests. Left: polarization (dashed lines) and power (solid lines) curves of Al-air cells assembled with different acidic electrolytes and AC1 and Pt/C cathodes. Blue lines: 50Xa, Green: 70Xa, Black: 90Xa, Red: 140Xa. Right: anodic, cathodic and full cell V/I curves of cells assembled with different electrolytes and cathodes. Blue lines: 50Xa, Green: 70Xa, Black: 90Xa, Red: 140Xa, Olive dashed: 70Xa_Pt/C. Discharge duration 600 s, rest time 60 s. (For interpretation of the references to colour in this figure legend, the reader is referred to the Web version of this article.)

hydrogel. This better result is due to a higher concentration of liquid solution in the gel, which guarantees greater conductivity and better contact with the cathodic and anodic surfaces, facilitating the transfer of charge, thus withstanding higher currents with more negative anodic and more positive cathodic potentials. On the contrary, in the range of currents considered in the tests, the 140Xa-cell potentials are always lower than those ones obtained with the other hydrogels due to the low liquid amount and poor electrode wettability. This result is also confirmed by the polarization-power curves carried out on the 140Xa-cells with both AC1 and Pt/C cathodes. For this reason, the 140Xa gel was not further investigated.

These electrochemical measurements have shown that the cells assembled with wood-derived platinum-free cathodes undoubtedly perform better. To gain insight into the electrochemical processes underlying the AC1 and Pt/C cathode functioning, three-electrode galvanostatic EIS analysis was performed at different discharge currents (Fig. 4) and during the discharge tests (Figs. 5 and 6).

The impedance measurements are usually carried out by potentiostatic control at a stationary state where AC potential is superimposed to the cell OCV. In this case, the current response is composed of both anodic and cathodic contributions. To get specific information on the cathodic processes during cell operation, impedance spectra may be acquired by setting the galvanostatic control on EIS measurements, imposing the WE on cathodes. Fig. 4 reports the Nyquist (top) and Bode (bottom) diagrams obtained from galvanostatic EIS measurements at different discharge currents effected on cells made with AC1 (left) and Pt/C (right) cathodes. These galvanostatic EIS measurements were carried out on cells discharged for 600 s at the same current density and with a 100 μA current amplitude perturbation. The EIS spectra of cells assembled with AC1 cathodes show scattered points at lower frequencies indicating that, for this system, the linearity conditions of the EIS analysis are not completely satisfied [37,38]. However, we believe that a 100 μA amplitude perturbation still allows a good S/N ratio which allows to deduce some of the fundamental features of the impedance spectra. In fact, we have verified that the increase of 100 μA on a 1 mA galvanostatic discharge on this galvanic cell produces a 10 mV decrease in the potential (Fig. S5) and that the impedance spectra on this system acquired with an amplitude of 200 μA (Fig. S6) show a better signal to noise ratio and reproduce essentially the same features as those in Fig. 4. For this reason, we selected 100 μA as a tradeoff perturbation value which does not significantly distort impedance spectra and gives good S/N signals [37].

In the Nyquist representation of impedance spectra, the width on the real axis of the depressed semicircle at higher frequencies corresponds to the charge transfer resistance (R_{ct}), while the spectral features at lower frequencies are related to mass transport phenomena [38]. Impedance spectra of both cathodes show features of the R_{ct} depressed semicircles at high frequencies and of mass diffusion phenomena at low frequencies [38]. Deviation from the ideal Warburg-diffusion phenomena may be due to the cathode porous microstructures [39].

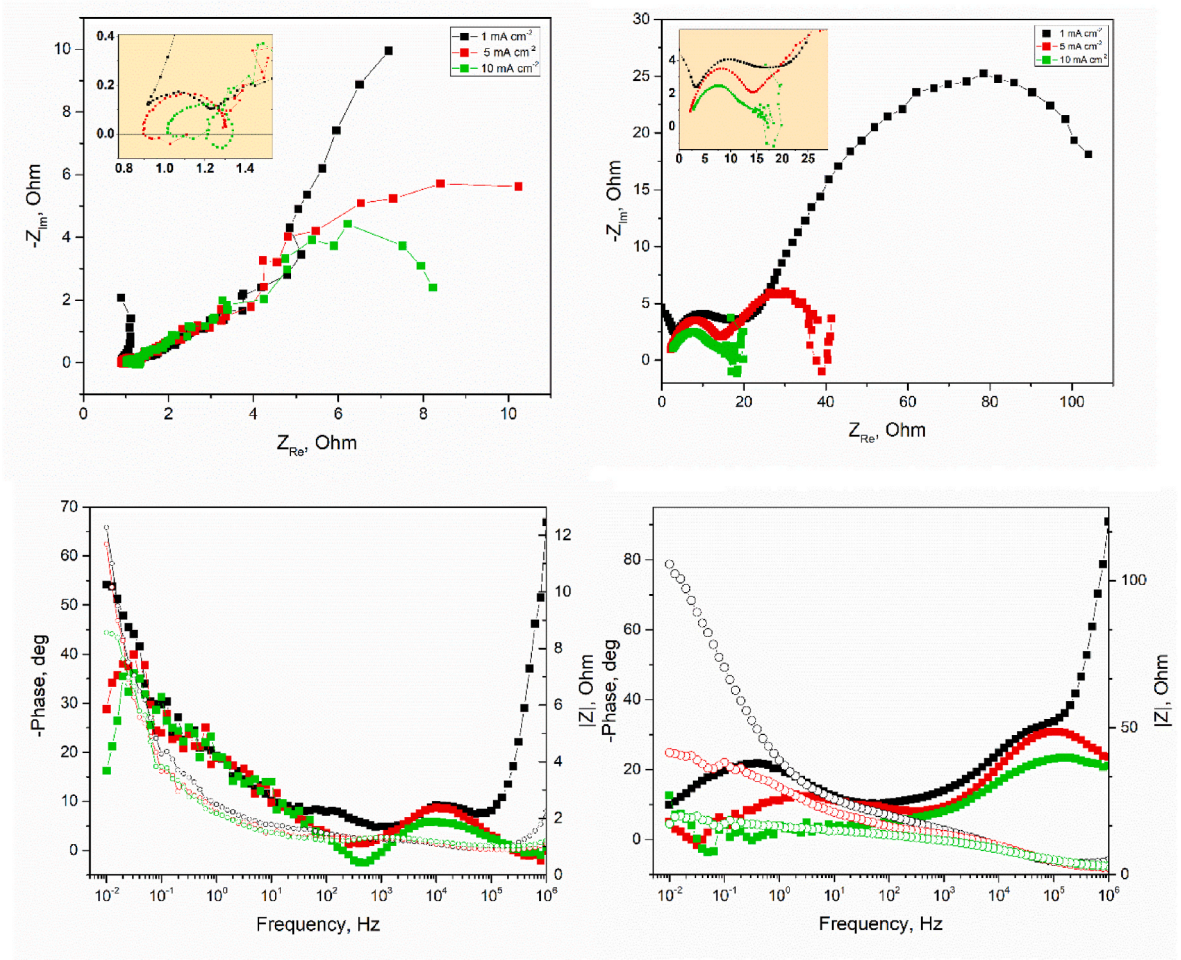

Fig. 4. Three-electrode galvanostatic impedance spectra at different discharge currents showed in the Nyquist (top) and Bode (bottom) representations of cells assembled with Pt/C (right) and AC1 (left) cathodes and 70Xa gel electrolyte. In black, red and green the data are related to 1, 5 and 10 mA cm^{-2}, respectively. In the Bode representation, the filled square and empty circles are data related to Phase and Z module, respectively. Each EIS analysis has been performed after 600 s discharge at the same currents. (For interpretation of the references to colour in this figure legend, the reader is referred to the Web version of this article.)

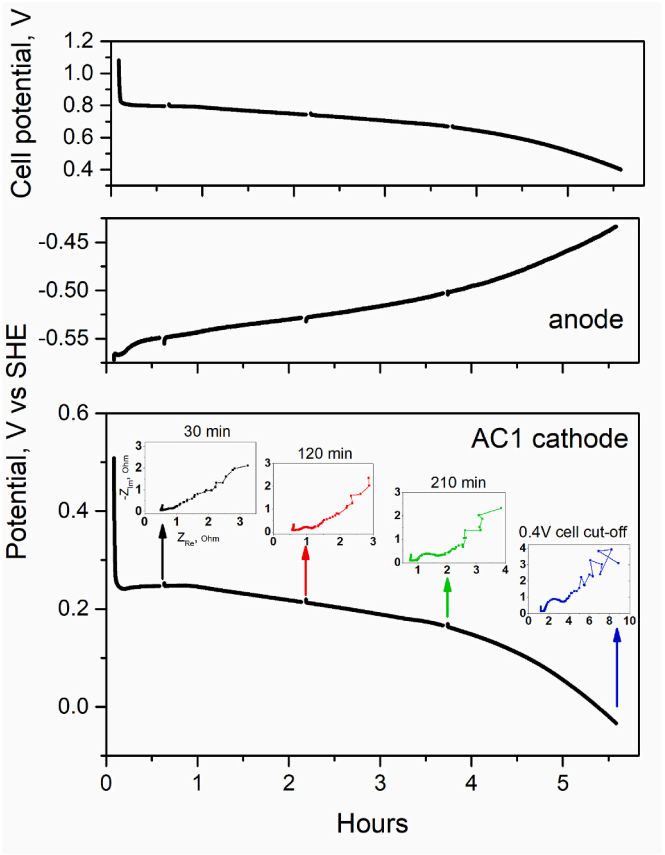

Fig. 5. Three electrode discharge test at 7 mA cm^{-2} current density with three-electrode galvanostatic EIS during discharge. 70Xa-cell with AC1 cathode. The insets in the cathodic potential layer are impedance spectra, in the Nyquist representation, acquired at different times from the start of discharge, i (y axis: Z_{Im}, Ohm. x axis: Z_{Re}, Ohm).

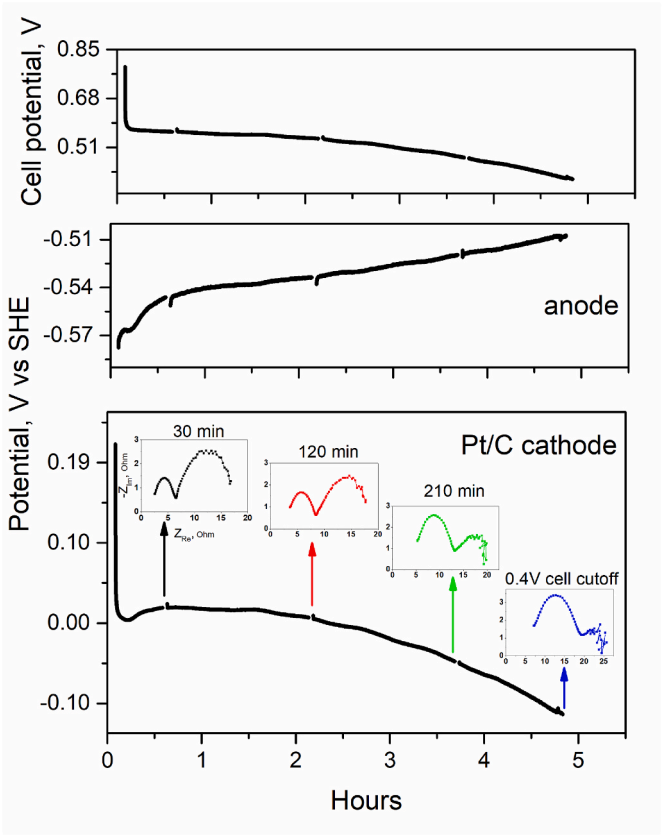

Fig. 6. Three-electrode discharge test at 7 mA cm^{-2} current density with three-electrode galvanostatic EIS during discharge. 70Xa-cell with Pt/C cathode. The insets in the cathodic potential layer are impedance spectra, acquired at different times from the start of discharge, in the Nyquist representation (y axis: Z_{Im}, Ohm. x axis: Z_{Re}, Ohm).

From Fig. 4, the R_{ct} of the Pt/C cathode depends on the discharge current density, as it could be expected due to the increase of charge amount available for the electrochemical reaction by increasing the current. Instead, from the AC1 EIS spectra, an inductive loop is clearly shown between 10^2 and 10^3 Hz (Fig. S6). This loop may alter the evaluation of the semicircle width, which is linked to the R_{ct}, so we cannot state to what extent in AC1 the R_{ct} depends on the current. Both cathodes show low frequency impedance features strongly dependent on the galvanostatic current. This may be due to the fact that these cells during discharge produce H_2O on cathode, by improving the diffusivity of ionic electroactive species. Anyway, from the spectra in Fig. 4 left, it is clear that the impedances associated with the R_{ct} are much lower than those associated with mass transport phenomena. Thus, in the AC1 cathode, mass transport appears to be the limiting stage for cathode efficiency. On the other hand, in the Pt/C cathode, the mass transport is relevant only at low current densities. It appears equally clear that all the impedances, both those associated with the R_{ct} and those of the transport phenomena, are much lower in the AC1 cathodes, therefore the wood-derived carbonaceous material is more effective for the ORRs and also offers less resistance to the transport of the electroactive species.

The cathode electrochemical processes during discharge tests have been highlighted through three-electrode galvanostatic EIS analysis as shown in Figs. 5 and 6. The discharge current density was set at 7 mA cm^{-2} for both cathodes. The Pt/C cathode shows two depressed semicircles, one attributable to the R_{ct}, at higher frequencies, while the other, at low frequencies, shows the characteristics of a finite diffusion phenomenon, in which the electroactive species move through the electrode [40]. During the discharge the amplitude of the semicircle at high frequencies (R_{ct}) tends to increase, most likely due to platinum catalyst degradation contacted with the acidic electrolyte [41], while the amplitude of the one at lower frequencies decreases, until it becomes a noisy signal.

The impedance spectra of the AC1 cathode are more complex due to the appearance of additional semicircles at medium-low frequencies (Fig. S7, left). Basically, the R_{ct} is very low and the mass transfer plays the most important role in the impedance spectra so that the R_{ct} features at higher frequency are slightly or not visible. The slope between 10^1 to 10^{-1} Hz is close to 45° (Fig. S7, left), highlighting the main contribution from semi-infinite diffusion phenomena with faradaic reaction occurring mainly on the electrode surface [40]. The appearance of additional semicircles between 10^1 to 10^3 Hz, with phase lower than 45° may be due to the complex geometry of the diffusion path because of the hierarchical porous structure of the wood-derived carbonaceous material [39]. The impedance of these diffusion processes increases during cell functioning probably due to clogging phenomena. Unequivocally, from Figs. 5 and 6, it emerges that the cathode made with carbonaceous material of natural origin maintains a more positive potential throughout the duration of the discharge. This lower overpotential can be explained by the lower impedances associated with the electrochemical and mass transport phenomena involved in the ORRs occurring on these materials.

From Nyquist spectra of both cathodes, the intercept with the x-axis, evaluating the electrolyte resistance, shifts toward higher impedance values. Thus, the cell failures, occurring after 5-h functioning in both cells at 7 mA cm^{-2}, are most likely due to the drying or clogging of the electrolyte which impede to electroactive species to be transported through the cathode active sites, even if, during the discharge, water is

produced with beneficial effect on the diffusion of electroactive species. In fact, due to the open structure of the cathode, the amount of liquid in the GPE evaporates during the measurements [19], affecting the cell overpotentials and the discharge duration, namely the cell capacity.

The capacity of 1 cm^2 button cells made with AC1 may be evaluated from Fig. 7a–b which report some discharge tests carried out up to the 0.2 V cutoff at 1 mA cm^{-2} and 10 mA cm^{-2}, respectively.

The cell capacities reasonably result to be 20–25 mAh cm^{-2}. The higher values found at 10 mA cm^{-2} are due to the reduced electrolyte evaporation because of shorter duration measurements. The electrolyte solution amount affects the cell capacity as well as the occurrence of the parasitic reaction, so that we found particularly noteworthy the capacity and potential values of 90Xa-cell at lower current densities.

The on-off cycle that simulates a real application of the cell is reported in Fig. 7c. The cycle was performed by discharging the 70Xa-cell with AC1 cathode at 1 mA cm^{-2} for 60 min ON and 60 min OFF. After 24 h, the cell presented a severe potential decrease until the cut-off (0.2 V). The comparison with Fig. 7a shows that a working period of 24 h produces the decrease of cell potential in both continuous and on-off cycle discharge, indicating that the main cause of cell performance decrease at low current (1 mA cm^{-2}) can be associated with the electrolyte drying process (Fig. 2d).

It is worth noting that, apart from the free-oxide-layer anode (Figs. S2–S4), the other cell components used in discharge or discharge on-off cycles are not reusable. In fact, as mentioned above, the electrolytes dry out and/or clog, and the cathodes lose the catalytic layer, which remains attached to the electrolyte, in the disassembly of the cell (Figs. S8–S12).

Fig. 8 reports the anodic efficiency (AE) evaluation as a function of polymer concentration and current density.

The 50Xa and 70Xa cells follow the trend expected for the liquid solutions. This is because the parasitic reaction (Eq. (4)) is competitive with the anode electrochemical reaction (Eq. (1)) and is unfavored at high current densities. Thus, in the 50Xa and 70Xa-cells, the anodic efficiency increases with the discharge current density. Instead, the anodic efficiency measured for the 90Xa-cell, in the investigated 1–10 mA cm^{-2} range, are always higher than the 80 %, reaching the outstanding 90 % value corresponding to 2682 mAh g^{-1} gravimetric capacity and a maximum energy density value of 2700 Wh Kg^{-1}. For comparison, as reported in a recent paper [42], the best gravimetric capacity of alkaline Al-air cells made with pure aluminum anode and 4M NaOH with 20 % glycerol added to electrolyte, is 2564 mAh g^{-1} (AE 86 %) with the maximum energy density value equal to 2102.6 Wh kg^{-1}. The fact that the gel with the highest concentration of xanthan, namely with the reduced concentration of free H^+ and Cl^-, responsible for aluminum corrosion in the xanthan-based acidic electrolytes [14], determine a flat trend of the anodic efficiency with the current density means that the electrochemical reaction is always favored at each current value.

4. Conclusions

Al-air cells made with acidic GPEs are electrochemical energy storage and conversion devices with great potentiality. Unlike alkaline cells, they do not produce, or produce much less, solid compounds by parasitic reaction and this allows greater cell discharge duration with cell capacity which results mainly affected by electrolyte evaporation. The corrosion control by the GPE itself, without the use of additives,

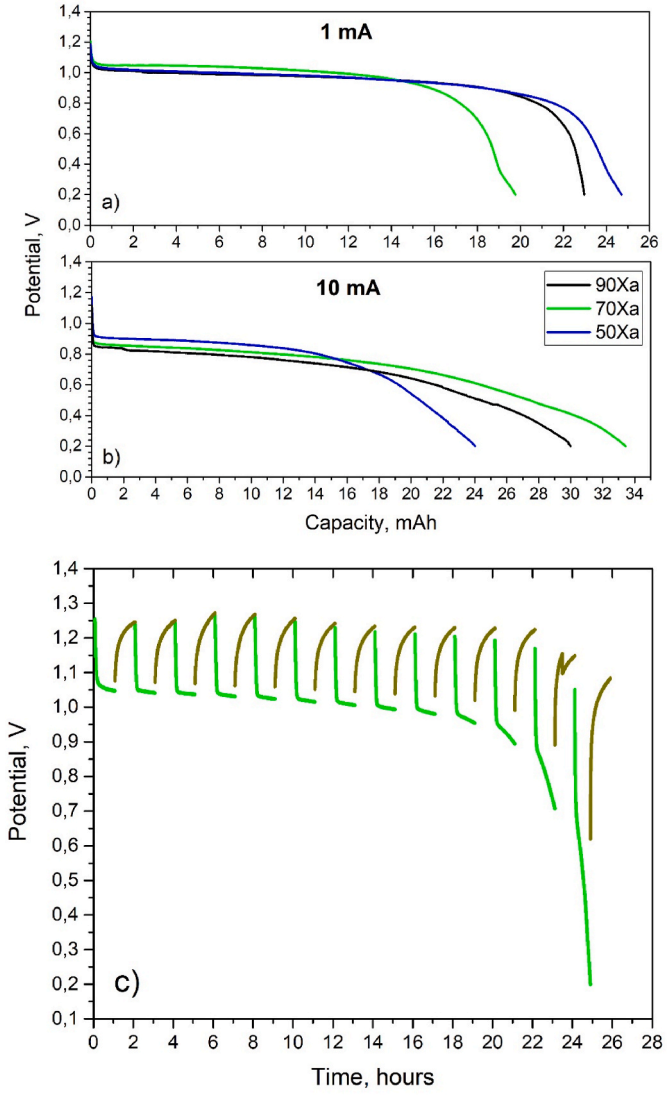

Fig. 7. a,b) Discharge curves of 50Xa, 70Xa and 90Xa-cells assembled with AC1 cathodes at 1 mA and 10 mA, respectively. c) On-off discharge cycle at 1 mA cm^{-2} on 70Xa cell with AC1 cathode. Cycles effected with 60 min-on (green lines) and 60 min-off (dark yellow lines). (For interpretation of the references to colour in this figure legend, the reader is referred to the Web version of this article.)

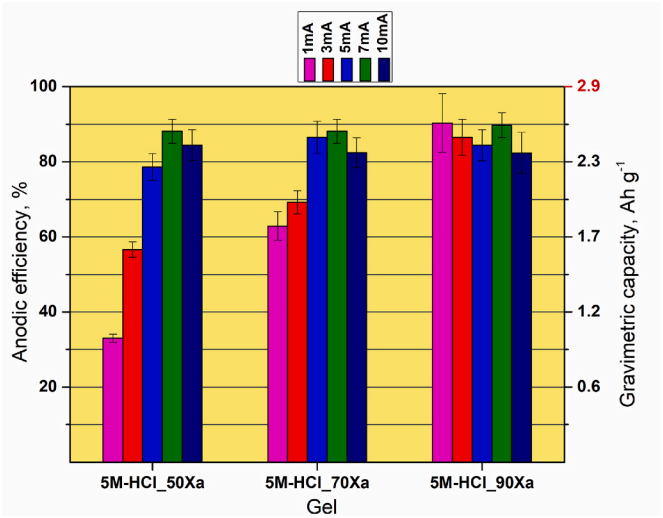

Fig. 8. Anodic efficiency/Gravimetric capacity measured after discharge test at various currents carried out on cells assembled with different gels and AC1 cathodes. The discharge duration varied between 1 h (data at 10 mA) and 6 h (1 mA). The theoretical capacity value is reported in red on the vertical right axis. (For interpretation of the references to colour in this figure legend, the reader is referred to the Web version of this article.)

guarantees the high anode utilization percentage. The use of more efficient and inexpensive cathodes, withstanding the ORR in acidic media, adds further value to this non-ordinary Al-air battery.

We demonstrated that the Al-air cells using xanthan-based acidic electrolytes and metal-free cathodes made of wood-derived carbonaceous materials present electrochemical performances superior to those assembled with the Pt/C cathodes. The electrochemical processes on the cathode have been highlighted by three-electrode galvanostatic EIS analysis. The cathodes made of wood-derived carbonaceous materials resulted characterized by very low ORR charge transfer resistance as well as low impedance to semi-infinite diffusion processes, other than good porosity and increased graphitization. Instead, the Pt/C cathode showed higher oxygen reduction R_{ct} which also increased during the cell functioning, presumably because of the catalyst degradation in acidic electrolytes.

These acidic Al-air cells show an outstanding 2682 mAh g^{-1} gravimetric capacity and a maximum energy density value of 2700 Wh Kg^{-1}. Improvements are expected with the creation of electrolytes that guarantee greater water retention capability. As primary batteries, the systems studied in our work could find application in low-power disposable devices, with significant advantages in terms of anodic metal consumption and cathode cost.

CRediT authorship contribution statement

M.F. Gaele: Writing – original draft, Methodology, Investigation, Data curation, Conceptualization. **P. Gargiulo:** Writing – review & editing, Methodology, Investigation, Data curation. **T.M. Di Palma:** Writing – review & editing, Writing – original draft, Supervision, Methodology, Investigation, Funding acquisition, Formal analysis, Data curation, Conceptualization.

Declaration of competing interest

The authors declare that they have no known competing financial interests or personal relationships that could have appeared to influence the work reported in this paper.

Acknowledgements

This work was supported by the Italian Ministry of Research, under the complementary actions to the NRRP “Fit4MedRob - Fit for Medical Robotics” Grant (# PNC0000007) – (Piano Nazionale Complementare (PNC) – Decreto Direttoriale n. 931 del 6 giugno 2022 – Avviso per la concessione di finanziamenti destinati ad iniziative di ricerca per tecnologie e percorsi innovativi in ambito sanitario e assistenziale, cod. PNC 0000007 – CUP B53C22006960001). All the authors also acknowledge the financial support project PRIN 2022PNRR – Cod. P20227BLHS, CUP B53D23025240001.

Preparation and characterization of the materials were carried out by using equipment of the Center of Excellence-Sustainable Energy Sources (CoE-SES) .

Appendix A. Supplementary data

Supplementary data to this article can be found online at https://doi.org/10.1016/j.jpowsour.2024.235784.

Data availability

Data will be made available on request.

References

[1] S.K. Gupta, J. Vishwakarma, A.K. Srivastava, C. Dhand, N. Dwivedi, Aluminum batteries: opportunities and challenges, Energy Storage Mater. (2024) 103538, https://doi.org/10.1016/j.ensm.2024.103538.

[2] X. Liu, H. Jiao, M. Wang, W.L. Song, J. Xue, S. Jiao, Current progresses and future prospects on aluminium–air batteries, Int. Mater. Rev. 67 (7) (2022) 734–764, https://doi.org/10.1080/09506608.2021.2006968.

[3] S. Ponnada, M.S. Kiai, R. Krishnapriya, R. Singhal, R.K. Sharma, Lithium-free batteries: needs and challenges, Energy Fuel. 36 (12) (2022) 6013–6026, https://doi.org/10.1021/acs.energyfuels.2c00569.

[4] M. Gao, R. Wang, X. Lu, Y. Fan, Z. Guo, Y. Wang, A highly reversible Sn-air battery possessing the ultra-low charging potential with the assistance of light, Angew. Chem. Int. Ed. (2024) e202407856, https://doi.org/10.1002/anie.202407856.

[5] Y. Zhou, S. Guo, Recent advances in cathode catalyst architecture for lithium–oxygen batteries, eScience 3 (4) (2023) 100123, https://doi.org/10.1016/j.esci.2023.100123.

[6] X. Wang, M. Yu, X. Feng, Electronic structure regulation of noble metal-free materials toward alkaline oxygen electrocatalysis, eScience 3 (4) (2023) 100141, https://doi.org/10.1016/j.esci.2023.100141.

[7] Z. Chang, X.B. Zhang, Introduction to metal–air batteries: theory and basic principles, in: Metal-Air Batteries: Fundamentals and Applications, Wiley-VCH Verlag GmbH & Co. KGaA, Weinheim, Germany, 2018, pp. 1–9, https://doi.org/10.1002/9783527807666.ch1.

[8] T.M. Di Palma, F. Migliardini, M.F. Gaele, P. Corbo, Aluminum-air Batteries with solid hydrogel electrolytes: effect of pH upon cell performance, Anal. Lett. 54 (1–2) (2021) 28–39, https://doi.org/10.1080/00032719.2019.1708923.

[9] Q. Wang, H. Miao, Y. Xue, S. Sun, S. Li, Z. Liu, Performances of an Al–0.15 Bi–0.15 Pb–0.035 Ga alloy as an anode for Al–air batteries in neutral and alkaline electrolytes, RSC Adv. 7 (42) (2017) 25838–25847, https://doi.org/10.1039/C7RA02918G.

[10] Y. Huang, L. Guo, Q. Zhang, W. Shi, W. Feng, F. Abbas, X. Zheng, S. Leng, Y. Qiang, V.S. Saji, Regulating the anode corrosion by a tryptophan derivative for alkaline Al–air batteries, Langmuir (2023), https://doi.org/10.1021/acs.langmuir.3c00032.

[11] Y. Wu, Y. Zhu, X. Li, D. Zhang, L. Gao, Enhanced performance of Al-0.02 Mg-0.01 Sn-0.004 Bi-0.003 in alloy as novel anode for Al-air batteries in alkaline electrolyte, J. Alloys Compd. 924 (2022) 166530, https://doi.org/10.1016/j.jallcom.2022.166530.

[12] H. Gupta, R.K. Singh, High-voltage nickel-rich NMC cathode material with ionic-liquid-based polymer electrolytes for rechargeable lithium-metal batteries, Chemelectrochem 7 (17) (2020) 3597–3605, https://doi.org/10.1002/celc.202000608.

[13] L. Balo, H. Gupta, S.K. Singh, V.K. Singh, A.K. Tripathi, N. Srivastava, R.K. Singh, Development of gel polymer electrolyte based on LiTFSI and EMIMFSI for application in rechargeable lithium metal battery with GO-LFP and NCA cathodes, J. Solid State Electrochem. 23 (2019) 2507–2518, https://doi.org/10.1007/s10008-019-04321-6.

[14] F. Migliardini, T.M. Di Palma, M.F. Gaele, P. Corbo, Solid and acid electrolytes for Al-air batteries based on xanthan-HCl hydrogels, J. Solid State Electrochem. 22 (2018) 2901–2916, https://doi.org/10.1007/s10008-018-4003-2.

[15] T.M. Di Palma, F. Migliardini, M.F. Gaele, P. Corbo, Physically cross-linked xanthan hydrogels as solid electrolytes for Al/air batteries, Ionics 25 (2019) 4209–4217, https://doi.org/10.1007/s11581-019-02965-y.

[16] EFSA Panel on Food Additives and Nutrient Sources added to Food (ANS), A. Mortensen, F. Aguilar, R. Crebelli, A. Di Domenico, M.J. Frutos, P. Galtier, D. Gott, U. Gundert-Remy, C. Lambré, J.C. Leblanc, Re-evaluation of xanthan gum (E 415) as a food additive, EFSA J. 15 (7) (2017) e04909, https://doi.org/10.2903/j.efsa.2017.4909.

[17] E.M. Nsengiyumva, P. Alexandridis, Xanthan gum in aqueous solutions: fundamentals and applications, Int. J. Biol. Macromol. 216 (2022) 583–604, https://doi.org/10.1016/j.ijbiomac.2022.06.189.

[18] S. Chaturvedi, S. Kulshrestha, K. Bhardwaj, R. Jangir, A review on properties and applications of xanthan gum, Microbial Polymers: Applications and Ecological Perspectives (2021) 87–107, https://doi.org/10.1007/978-981-16-0045-6_4.

[19] M.F. Gaele, P. Gargiulo, T.M. Di Palma, Eco-sustainable aluminum-air batteries, Anal. Lett. (2024) 1–18, https://doi.org/10.1080/00032719.2024.2345745.

[20] T.M. Di Palma, F. Migliardini, D. Caputo, P. Corbo, Xanthan and κ-carrageenan based alkaline hydrogels as electrolytes for Al/air batteries, Carbohydr. Polym. 157 (2017) 122–127, https://doi.org/10.1016/j.carbpol.2016.09.076.

[21] Y. Wang, W. Pan, S. Luo, X. Zhao, H.Y. Kwok, X. Xu, D.Y. Leung, High-performance solid-state metal-air batteries with an innovative dual-gel electrolyte, Int. J. Hydrogen Energy 47 (33) (2022) 15024–15034, https://doi.org/10.1016/j.ijhydene.2022.03.011.

[22] Q. Zhao, P. Wu, D. Sun, H. Wang, Y. Tang, A dual-electrolyte system for highly efficient Al–air batteries, Chem. Commun. 58 (20) (2022) 3282–3285, https://doi.org/10.1039/D1CC07044D.

[23] L. Wang, R. Cheng, C. Liu, M.C. Ma, W. Wang, G. Yang, M.K.H. Leung, F. Liu, S. P. Feng, Trielectrolyte aluminum-air cell with high stability and voltage beyond 2.2 V, Materials Today Physics 14 (2020) 100242, https://doi.org/10.1016/j.mtphys.2020.100242.

[24] M.F. Gaele, F. Migliardini, T.M. Di Palma, Dual solid electrolytes for aluminium-air batteries based on polyvinyl alcohol acidic membranes and neutral hydrogels, J. Solid State Electrochem. 25 (2021) 1207–1216, https://doi.org/10.1007/s10008-021-04900-6.

[25] M.F. Gaele, T.M. Di Palma, Rechargeable aluminum-air batteries based on aqueous solid-state electrolytes, Energy Technol. 10 (4) (2022) 2101046, https://doi.org/10.1002/ente.202101046.
[26] M.F. Gaele, V. Califano, T.M. Di Palma, Efficient cathodes for quasi-solid-state aluminum-air batteries, Ionics 29 (4) (2023) 1447–1458, https://doi.org/10.1007/s11581-023-04896-1.
[27] European Commission, Critical raw materials. https://ec.europa.eu/growth/sectors/raw-materials/specific-interest/critical_en, 2020.
[28] M.P. Martínez-Hernando, E. García-Franco, D. Bolonio, M.F. Ortega, M.J. García-Martínez, Life cycle sustainability assessment of the platinum supply chain in the European Union, Sustain. Prod. Consum. 46 (2024) 679–689, https://doi.org/10.1016/j.spc.2024.03.017.
[29] M.A. Yahya, Z. Al-Qodah, C.Z. Ngah, Agricultural bio-waste materials as potential sustainable precursors used for activated carbon production: a review, Renew. Sustain. Energy Rev. 46 (2015) 218–235, https://doi.org/10.1016/j.rser.2015.02.051.
[30] Y. Tao, R. Zhang, W. Xu, Z. Bai, Y. Zhou, S. Zhao, Y. Xu, D. Yu, Rheological behavior and microstructure of release-controlled hydrogels based on xanthan gum crosslinked with sodium trimetaphosphate, Food Hydrocolloids 52 (2016) (2016) 923–933, https://doi.org/10.1016/j.foodhyd.2015.09.006.
[31] V.G. Artemov, A.A. Volkov, N.N. Sysoev, Conductivity of aqueous HCl, NaOH and NaCl solutions: is water just a substrate? Europhys. Lett. 109 (2) (2015) 26002 https://doi.org/10.1209/0295-5075/109/26002.
[32] J. Wang, C.X. Zhao, J.N. Liu, D. Ren, B.Q. Li, J.Q. Huang, Q. Zhang, Quantitative kinetic analysis on oxygen reduction reaction: a perspective, Nano Mater Sci 3 (3) (2021) 313–318, https://doi.org/10.1016/j.nanoms.2021.03.006.
[33] N. Daems, T. Breugelmans, I.F. Vankelecom, P.P. Pescarmona, Influence of the composition and preparation of the rotating disk electrode on the performance of mesoporous electrocatalysts in the alkaline oxygen reduction reaction, Chemelectrochem 5 (1) (2018) 119–128, https://doi.org/10.1002/celc.201700907.
[34] E.M. Stuve, Overpotentials in electrochemical cells, in: G. Kreysa, Ota Ki, R. F. Savinell (Eds.), Encyclopedia of Applied Electrochemistry, Springer, New York, 2014, pp. 1445–1453, https://doi.org/10.1007/978-1-4419-6996-5_330.
[35] K. Kinoshita, Carbon: Electrochemical and Physicochemical Properties, 1988. United States. ISBN: 978-0-471-84802-8.
[36] B. Kwiecinska, I. Suarez-Ruiz, C. Paluszkiewicz, S. Rodriques, Raman spectroscopy of selected carbonaceous samples, Int. J. Coal Geol. 84 (3–4) (2010) 206–212, https://doi.org/10.1016/j.coal.2010.08.010.
[37] J.J. Giner-Sanz, E.M. Ortega, V. Pérez-Herranz, Optimization of the perturbation amplitude for EIS measurements using a total harmonic distortion based method, J. Electrochem. Soc. 165 (10) (2018) E488, https://doi.org/10.1149/2.1021810jes.
[38] X.Z. Yuan, C. Song, H. Wang, J. Zhang, Electrochemical Impedance Spectroscopy in PEM Fuel Cells: Fundamentals and Applications, vol. 13, Springer London, London, 2010, https://doi.org/10.1007/978-1-84882-846-9, 420.
[39] S.J. Cooper, A. Bertei, D.P. Finegan, N.P. Brandon, Simulated impedance of diffusion in porous media, Electrochim. Acta 251 (2017) 681–689, https://doi.org/10.1016/j.electacta.2017.07.152.
[40] A.C. Lazanas, M.I. Prodromidis, Electrochemical impedance spectroscopy - a tutorial. https://doi.org/10.1021/acsmeasuresciau.2c00070ACSMeasurementScienceAu, 2023, 3(3), pp.162–193.
[41] Y. Furuya, T. Mashio, A. Ohma, M. Tian, F. Kaveh, D. Beauchemin, G. Jerkiewick, Influence of electrolyte composition and pH on platinum electrochemical and/or chemical dissolution in aqueous acidic media, ACS Catal. 5 (4) (2015) 2605–2614, https://doi.org/10.1021/cs5016035.
[42] T.H. Pham, W.H. Lee, J.H. Byun, J.G. Kim, Improving the performance of primary aluminum-air batteries through suppressing water activity by hydrogen bond-rich glycerol solvent additive, Energy Storage Mater. 55 (2023) 406–416, https://doi.org/10.1016/j.ensm.2022.12.012.